Preparation and control of electronic wave packets in neutral molecules via attosecond x-ray processes

Emanuele Rossi [1,2,3,*] Stasis Chuchurka,[1,2,†] Kaushik D. Nanda,[4,‡] Anna I. Krylov [4] Nina Rohringer,[2,1,3,§] and Robin Santra [2,1,3,‖]

[1]*Department of Physics, University of Hamburg, Hamburg, Germany*
[2]*Center for Free-Electron Laser Science CFEL, Deutsches Elektronen-Synchrotron DESY, Hamburg, Germany*
[3]*The Hamburg Centre for Ultrafast Imaging, Hamburg, Germany*
[4]*Department of Chemistry, University of Southern California, Los Angeles, California 90089, USA*

(Received 18 June 2026; accepted 20 October 2026; published 6 November 2026)

We present a perturbative framework for computing the dynamics of an electronic wave packet launched by an attosecond x-ray pulse in a neutral molecule. The x-ray pulse excites the molecule via both x-ray absorption and impulsive stimulated x-ray Raman scattering (ISXRS), coherently populating both the core-excited states and valence-excited states. We describe the electronic structure within the equation-of-motion coupled-cluster framework, adopting a compact representation of the sum-over-states expression characterizing the second-order perturbative description of ISXRS. We study the coherent electronic dynamics in carbonyl sulfide and oxazole utilizing the time-dependent difference electron density, decomposing it in terms of its perturbative components. While the core-excited components dominate the initial stages of the dynamics, the valence-excited components dominate the electronic dynamics on a longer timescale. The pulse polarization controls the symmetry of the states included in the wave packet. We show how the spatial symmetry of the states plays a role in shaping the spatial properties of charge migration. The atomic specificity of the ISXRS process translates directly into the initial localization of the wave packet. This determines the starting point of charge migration, shaping its subsequent evolution.

DOI: 10.1103/sprw-mrh2

I. INTRODUCTION

The emergence of light sources capable of producing ultrashort pulses has allowed the study of the dynamics of a photochemical process with ever higher time resolution. Pulses of femtosecond duration gave access to the timescale of nuclear motion; this enabled the reconstruction and control of the dynamics of a photochemical reaction on a femtosecond timescale, establishing the field of femtochemistry [1].

The introduction of attosecond pulses [2,3] pushed the time resolution to that of electronic motion, introducing an electronic timescale to the study of a photochemical reaction [4,5]. The intramolecular distribution of the electrons plays a crucial role in shaping the molecular bonding network: Owing to the coupling between the nuclei and the electrons, a reorganization of the electronic distribution can influence the nuclear dynamics and potentially route the chemical process on a particular pathway [6–9]. Based on this hypothesis, the idea of attochemistry has emerged [10], which proposes the control of a chemical process using the properties of an attosecond pulse to steer the electronic dynamics.

The reorganization of the electronic distribution underlying attochemistry is based on a purely electronic process, commonly known as charge migration [11,12]. As shown in Fig. 1(a), charge migration can be launched via a broadband excitation, which prepares a coherent superposition of electronic states, i.e., an electronic wave packet (WP) [13]. The change of the electronic density underlying charge migration corresponds to the time evolution of the superposition. Due to the high photon energies of the attosecond pulses, which often exceed the molecular ionization threshold, the pioneering studies in attochemistry considered a photoionization process to prepare the electronic WP [9,11,13–17]. However, since fundamental photochemical reactions (such as those involved in vision or photosynthesis [18]) rely on photoexcitation, the focus of recent studies has moved towards electronic dynamics in neutral molecules [19,20].

Contributing to this direction of research, we theoretically study charge migration in a neutral molecule, preparing the electronic WP with a broadband, attosecond x-ray pulse. In particular, we consider an attosecond x-ray pulse with an intensity similar to that achievable by an x-ray free-electron

*Present address: DTU Chemistry, Technical University of Denmark, Kemitorvet 207, 2800 Kongens Lyngby, Denmark.
†Present address: Institute of Physical Chemistry, Friedrich Schiller University Jena, Jena, Germany.
‡Present address: Q-Chem, Inc., 6601 Owens Drive, Suite 240, Pleasanton, CA 94588, USA.
§Contact author: nina.rohringer@desy.de
‖Contact author: robin.santra@cfel.de

Published by the American Physical Society under the terms of the Creative Commons Attribution 4.0 International license. Further distribution of this work must maintain attribution to the author(s) and the published article's title, journal citation, and DOI.

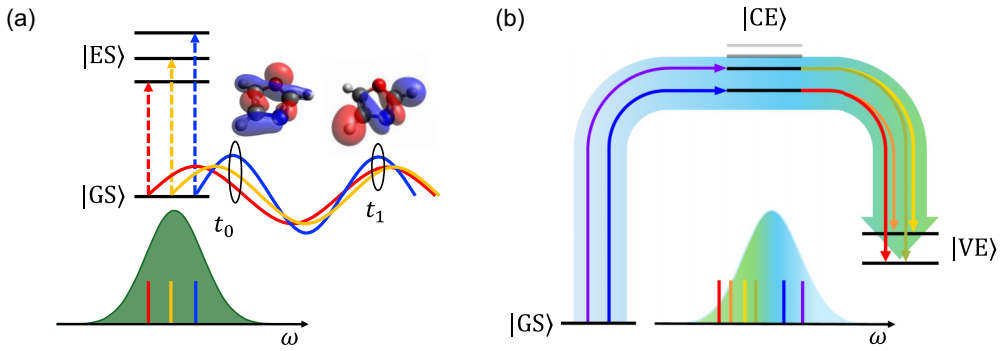


FIG. 1. Preparation of an electronic WP, charge migration, and schematic description of the ISXRS process. (a) Coherent excitation of the system from the ground state |GS⟩ to a manifold of excited states |ES⟩. The time evolution of the coherent superposition corresponds to the motion of the electronic density known as charge migration. (b) Schematic view of the ISXRS excitation with a broadband x-ray pulse. The manifold of core-excited and valence-excited states are indicated as |CE⟩ and |VE⟩, respectively. The arrows connecting |GS⟩ and |CE⟩ refer to the x-ray absorption step; the arrows connecting |CE⟩ and |VE⟩ refer to the x-ray stimulated emission step. Their coloring scheme corresponds to the respective absorbed and emitted frequencies, indicated by the colored bars contained within the pulse bandwidth.

laser (XFEL) [21]. The characteristics of this pulse make it possible to coherently populate the electronic states of the molecule in an atom-specific way [22]. Here we populate both the core-excited and the valence-excited states. The latter can be populated by exploiting the high intensity of the pulse, which gives access to nonlinear spectroscopic techniques such as impulsive stimulated x-ray Raman scattering (ISXRS) [23–26]. This technique was experimentally demonstrated in both atomic [27] and molecular systems [28–31]. A schematic description of this process [see Fig. 1(b)] relies on a sequence of two steps: an x-ray absorption (light blue background), which excites the molecule from its ground state to a manifold of core-excited states, and an x-ray stimulated emission (green background), which radiatively deexcites the molecule to a manifold of valence-excited states. Performing an ISXRS excitation using an x-ray pulse with a sufficiently large bandwidth, so that both the absorbed and emitted photon energies are contained within its spectrum, prepares a coherent superposition of the ground state and valence-excited states. The properties of such a superposition are atom specific and can be regulated by tuning the x-ray pulse [32–35].

The accurate modeling of the excitation and the electronic dynamics represents a theoretical challenge for electronic-structure theory and a fundamental component in the development of attochemistry. A wealth of time-dependent electronic-structure methods have been developed to tackle this challenge. Some examples are time-dependent density-functional theory [36–38], time-dependent configuration-interaction methods [39–44], multiconfiguration time-dependent Hartree methods [45–48], time-dependent Hartree-Fock methods [49], standard [50] and restricted [51] variants of time-dependent active-space self-consistent-field methods, time-dependent multiconfiguration self-consistent-field methods [52], methods based on the algebraic adiabatic construction [53–55], time-dependent coupled-cluster methods [56–60], and time-dependent equation-of-motion coupled-cluster (EOM-CC) methods [61–64].

Here we adopt an approach based on EOM-CC theory [65,66], which offers a rigorous framework for describing the molecular electronic structure and the x-ray spectroscopic properties [67]. In particular, we expand the electronic WP in a basis of EOM-CC states, approximating the corresponding time-dependent probability amplitudes through time-dependent perturbation theory. The corresponding perturbative expressions contain the resonant inelastic x-ray scattering (RIXS) transition moment, which is characterized by a sum over states, formally extending over the whole molecular spectrum.

The common approach to the calculation of the RIXS moment resorts to its truncation to a manifold of presumably dominant terms [68,69]; while this presents practical advantages, the loss of accuracy connected to the truncation of the sum over states is difficult to assess *a priori*. Here we make use of the EOM-CC implementation by Nanda *et al.* [70], which reformulates the RIXS transition moment in a closed form within damped response theory. This approach formally avoids the truncation of the sum over core-excited states. By integrating the nontruncated formulation of the RIXS transition moments in the calculation of the ISXRS probability amplitudes, we aim at improving the description of the ISXRS excitation (in the perturbative regime) compared to previous works [32–34,64], which included only a limited set of core-excited states in the manifold of intermediate states.

Within this framework, we study charge migration launched by an attosecond x-ray pulse in a neutral molecule by observing the changes in its time-dependent difference electron density (obtained by subtracting the ground-state electron density from the time-dependent electron density). In particular, we examine the relative contributions provided by the core and valence excitations by decomposing the time-dependent difference electron density in terms of its perturbative components. We perform this analysis in carbonyl sulfide (OCS) and oxazole, studying the properties of charge migration and how they are influenced by the pulse polarization and the inner-shell edge chosen for the x-ray excitation.

The paper is organized as follows. In Sec. II we present the perturbative description of the electronic WP and the details of its implementation within EOM-CC theory. In Sec. III A we present the perturbative decomposition of the time-dependent difference electron density in OCS, describing its hierarchy and spatial contributions. In Sec. III B we describe the valence-electron dynamics excited by ISXRS in OCS and

how it is affected by the x-ray polarization. In Sec. III C we describe the valence electron dynamics excited by ISXRS in oxazole and its atom-specific properties. In Sec. IV we summarize our work and discuss our conclusions.

II. THEORETICAL METHODS

In this section we employ atomic units. Throughout, we assume the nuclei to be clamped to their equilibrium positions. We describe the dynamics of the electronic system according to the semiclassical Hamiltonian

$$\hat{H}(t) = \hat{H}_{\mathrm{el}} - \hat{\boldsymbol{\mu}} \cdot \boldsymbol{E}(t). \tag{1}$$

The term $\hat{H}_{\mathrm{el}}$ is the nonrelativistic electronic Hamiltonian [71], while $\hat{\boldsymbol{\mu}}$ is the electric dipole operator. The classical electric field

$$\boldsymbol{E}(t) = \boldsymbol{\epsilon} E(t) \cos(\omega_f t) \tag{2}$$

represents the incoming pulse of Gaussian envelope $E(t)$, carrier frequency ω_f, and polarization $\boldsymbol{\epsilon}$. Since we consider only linearly polarized x-ray pulses, $\boldsymbol{\epsilon}$ is a real-valued vector.

We represent the WP $|\Psi(t)\rangle$ as a superposition of eigenstates of $\hat{H}_{\mathrm{el}}$. In particular, we focus on the states of the neutral molecule, considering the ground state $|\psi_g\rangle$, the core-excited states $|\psi_c\rangle$, and the valence-excited states $|\psi_v\rangle$. Assuming that the resonant enhancement makes the excitation pathways dominant over the photoionization pathways, we exclude the core-ionized and valence-ionized states from the expansion. Based on these assumptions, we expand $|\Psi(t)\rangle$ as

$$|\Psi(t)\rangle = \left[1 + a_g^{(2)}(t)\right]|\psi_g\rangle + \sum_c a_c^{(1)}(t) e^{-i(\omega_{cg} - i\Gamma_c/2)t}|\psi_c\rangle + \sum_v a_v^{(2)}(t) e^{-i(\omega_{vg} - i\Gamma_v/2)t}|\psi_v\rangle. \tag{3}$$

The superscripts added to the probability amplitudes in this expression indicate the leading order in the perturbation $\hat{\boldsymbol{\mu}} \cdot \boldsymbol{E}(t)$ to which each amplitude must be computed in order to obtain a (potentially) nonvanishing contribution. Since we consider resonant x-ray excitations, second-order corrections to the amplitudes associated with core-excited states may be neglected.

The probability amplitudes $a_c^{(1)}(t)$ and $a_v^{(2)}(t)$ are modulated by exponential factors which control their oscillation (at frequencies proportional to the excitation energies ω_{cg} and ω_{vg}, respectively) and exponential decay, which accounts for the spontaneous relaxation of the excited states. The parameter Γ corresponds to the rate of decay, which is related to the state's mean lifetime $\tau = 1/\Gamma$. We consider the same value of Γ_c for all core-excited states, choosing a value of 0.0052 a.u. (0.140 eV) for excitations at the O K edge [72], 0.0049 a.u. (0.132 eV) for excitations at the N K edge [73], and 0.0039 a.u. (0.105 eV) for excitations at the S L_1 edge [74]. Since τ_v is much larger than τ_c [75] and we study the dynamics in a time window of a few femtoseconds after the excitation, we consider Γ_v equal to zero for all the valence-excited states.

The first-order amplitudes

$$a_c^{(1)}(t) = \frac{1}{\sqrt{2\pi}} \int_0^\infty d\omega \frac{e^{i(\omega_{cg} - \omega - i\Gamma_c/2)t}}{\omega_{cg} - \omega - i\frac{\Gamma_c}{2}} E(\omega) \boldsymbol{\epsilon} \cdot \boldsymbol{\mu}_{cg} \tag{4}$$

describe the coherent population of the core-excited states upon absorption of an x-ray photon. Here $\boldsymbol{\mu}_{cg}$ represents the transition dipole moment between the ground state and the core-excited state; $E(\omega)$ corresponds to the Fourier transform of the pulse in Eq. (2), multiplied by the polarization vector $\boldsymbol{\epsilon}$. The second-order contributions $a_v^{(2)}(t)$ and $a_g^{(2)}(t)$ describe the coherent population of the valence-excited states (via ISXRS) and the depopulation of the ground state upon excitation, respectively. They are given by

$$a_k^{(2)}(t) = \frac{1}{2\pi} \int_0^\infty d\omega_p \int_0^\infty d\omega_d \frac{e^{i(\omega_{kg} - \omega_p + \omega_d - i\Gamma_k/2)t}}{\omega_{kg} - \omega_p + \omega_d - i\frac{\Gamma_k}{2}} \times E(\omega_p) E(\omega_d) M_{kg}(\omega_p, \omega_d), \tag{5}$$

with $k \in v, g$. Here the term $M_{kg}(\omega_p, \omega_d)$ corresponds to the second-order transition moment of the form

$$M_{kg}(\omega_p, \omega_d) = \sum_m \left(\frac{(\boldsymbol{\epsilon}_d \cdot \boldsymbol{\mu}_{km})(\boldsymbol{\epsilon}_p \cdot \boldsymbol{\mu}_{mg})}{\omega_{mg} - \omega_p - i\frac{\Gamma_m}{2}} + \frac{(\boldsymbol{\epsilon}_p \cdot \boldsymbol{\mu}_{km})(\boldsymbol{\epsilon}_d \cdot \boldsymbol{\mu}_{mg})}{\omega_{mg} + \omega_d - i\frac{\Gamma_m}{2}} \right), \tag{6}$$

where the sum over states formally extends over the whole spectrum of $\hat{H}_{\mathrm{el}}$. This expression is commonly found in the Kramers-Heisenberg dispersion formula [76] and the description of the RIXS process [77]. Owing to the resonant enhancement at x-ray frequencies, the contributions from the core-excited states play a dominant role in the sum over states in Eq. (6). Accordingly, we limit the sum over states to a sum over core-excited states. Instead of truncating the sum over core-excited states to a manifold of core-excited states [32–34,64,68,69], we use its closed-form reformulation within damped response theory, as presented in Ref. [70] and implemented in Q-CHEM 6.1 [78].

A. Perturbative decomposition of the electronic density matrix

To obtain a clearer description of its coherent properties, we represent the superposition state in terms of its density matrix, $\hat{\rho}(t) = |\Psi(t)\rangle\langle\Psi(t)|$. By substituting the expansion in Eq. (3) in the definition of $\hat{\rho}(t)$, we write the perturbative expansion of the density-matrix elements as

$$\rho_{nm}^{(N+M)}(t) = a_n^{(N)}(t) a_m^{(M)^*}(t) e^{-i\{\omega_{mn} - i[(\Gamma_m + \Gamma_n)/2]\}t}. \tag{7}$$

Here n and m denote electronic states, while N and M represent the perturbative orders of the probability amplitudes in Eq. (3); the sum $N + M$ gives the order of the corresponding density-matrix element. Having expanded the probability amplitudes to leading second order, the perturbative expansion of the density-matrix elements contains terms up to fourth order. The latter expansion is however complete only up to leading second order, which we adopt as our truncation threshold. As a consequence, the populations of the valence-excited states are neglected, while those of the ground and core-excited states are included. The ground-state population is given by

$$\rho_{gg}(t) \approx 1 + \rho_{gg}^{(2)}(t) = 1 + 2\,\mathrm{Re}\left[a_g^{(2)}(t)\right], \tag{8}$$

where the second term represents the depopulation of the ground state, while the populations of the core-excited states

are obtained via

$$\rho_{cc}(t) \approx \rho_{cc}^{(2)}(t) = a_c^{(1)}(t) a_c^{(1)^*}(t) e^{-\Gamma_c t}. \tag{9}$$

According to the same criterion, the coherences $\rho_{vv'}(t)$ between valence-excited states are neglected since their expansion contains only terms to leading fourth order. The only nonvanishing coherences are those between the ground state and the core-excited states,

$$\rho_{cg}(t) \approx \rho_{cg}^{(1)}(t) = a_c^{(1)}(t) e^{-i\omega_{cg}t} e^{-(\Gamma_c/2)t}, \tag{10}$$

between core-excited states,

$$\rho_{cc'}(t) \approx \rho_{cc'}^{(2)}(t) = a_c^{(1)}(t) a_{c'}^{(1)^*}(t) e^{-i\omega_{cc'}t} e^{-\Gamma_c t}, \tag{11}$$

and between the ground state and the valence-excited states,

$$\rho_{vg}(t) \approx \rho_{vg}^{(2)}(t) = a_v^{(2)}(t) e^{-i\omega_{vg}t} e^{-(\Gamma_v/2)t}. \tag{12}$$

B. Pulse properties and one-body observables within the perturbative model

An advantage of the perturbative approach is the possibility of decoupling the calculation of the electronic structure from the definition of the light field. This provides complete flexibility in the selection of the pulse, enabling the exploration of theoretical questions or simulations of realistic experimental conditions. For example, the stochastic nature of XFEL pulses can be considered by substituting the field $E(\omega)$ [see Eq. (4)] in first-order terms of the density matrix with the corresponding ensemble average $\langle E(\omega)\rangle$ and the product $E(\omega_p)E(\omega_d)$ [see Eq. (5)] in second-order terms of the density matrix with the Fourier transform of the first-order correlation function [79–81],

$$\langle E(\omega_p)E(\omega_d)\rangle = \mathcal{F}\{G^{(1)}(t,t')\}. \tag{13}$$

The time evolution of the electronic density matrix and its perturbative decomposition may be used to determine the time evolution of the expectation value of any observable. Specifically, for a one-particle observable $\hat{A}$, we can compute the matrix representation of the observable in direct correspondence with the elements of the electronic density matrix

$$A_{nm} = \sum_{pq} \gamma_{pq}^{nm} A_{pq}, \tag{14}$$

where $\gamma_{pq}^{nm} = \langle\psi_m|\hat{c}_q^\dagger \hat{c}_p|\psi_n\rangle$ (here assumed to be real) represents the one-particle reduced density matrix (1RDM), and the indices p and q correspond to a basis of one-particle functions, e.g., the canonical molecular-orbital basis. The time evolution of the expectation value of the observable is then given by

$$\langle A\rangle(t) = \sum_{nm} \rho_{mn}(t) A_{nm}. \tag{15}$$

In this work we choose the time-dependent electron density $\rho(\boldsymbol{r},t)$ as the observable by considering

$$A_{pq} = \phi_p(\boldsymbol{r})\phi_q(\boldsymbol{r}), \tag{16}$$

where $\phi_p(\boldsymbol{r})$ and $\phi_q(\boldsymbol{r})$ correspond to (real-valued) canonical molecular orbitals. The analysis of $\rho(\boldsymbol{r},t)$ allows us to obtain a direct, spatially resolved picture of the changes in the electronic distribution upon excitation of the electronic WP, while offering a connection to the properties of spectroscopic observables [82]. Due to the perturbative nature of the excitation, $\rho(\boldsymbol{r},t)$ is dominated by the (time-independent) ground-state electron density $\rho_{gg}(\boldsymbol{r})$. To analyze the changes in the electron density due to the excitation, we consider the difference density

$$\Delta\rho(\boldsymbol{r},t) = \rho(\boldsymbol{r},t) - \rho_{gg}(\boldsymbol{r}). \tag{17}$$

The perturbative expansion of the density matrix, with components as given in Eqs. (8)–(12), leads to the following expansion of the difference density:

$$\begin{aligned}\Delta\rho(\boldsymbol{r},t) \approx & \underbrace{\sum_c \rho_{cc}^{(2)}(t)\rho_{cc}(\boldsymbol{r}) + \rho_{gg}^{(2)}(t)\rho_{gg}(\boldsymbol{r})}_{\Delta_{cg}(\boldsymbol{r},t)} \\ & + \underbrace{\sum_c 2\,\mathrm{Re}\big[\rho_{cg}^{(1)}(t)\big]\rho_{gc}(\boldsymbol{r})}_{\rho_{cg}(\boldsymbol{r},t)} \\ & + \underbrace{\sum_v 2\,\mathrm{Re}\big[\rho_{vg}^{(2)}(t)\big]\rho_{gv}(\boldsymbol{r})}_{\rho_{vg}(\boldsymbol{r},t)} \\ & + \underbrace{\sum_{c'>c} 2\,\mathrm{Re}[\rho_{cc'}^{(2)}(t)]\rho_{c'c}(\boldsymbol{r})}_{\rho_{cc'}(\boldsymbol{r},t)}.\end{aligned} \tag{18}$$

Here each contribution to $\Delta\rho(\boldsymbol{r},t)$ maps to a perturbative component of the electronic density matrix. The populations and coherences act as time-dependent weights for their spatial counterparts, which correspond to the state densities and the transition densities, respectively.

C. Implementation within EOM-CC theory

We calculate the (state and transition) electron densities in Eq. (18) and the transition moments in Eqs. (4) and (5) within EOM-CC theory, which provides an accurate framework for the calculation of x-ray transition properties [67]. The calculation of the components of $\Delta\rho(\boldsymbol{r},t)$ associated with the coherences requires special attention, which is related to the non-Hermitian nature of EOM-CC theory. In standard quantum mechanics, the matrix element $\mathcal{O}_{nm}$ of a generic operator $\hat{\mathcal{O}}$ is defined in terms of an orthonormal bra and ket couple, i.e., $\mathcal{O}_{nm} = \langle\psi_n|\hat{\mathcal{O}}|\psi_m\rangle$. Within the non-Hermitian EOM-CC framework, biorthonormal left bras and right kets are computed, which leads to the appearance of the two distinct matrix elements [65]

$$\mathcal{O}_{n\leftarrow m} = \big\langle\psi_n^L\big|\hat{\mathcal{O}}\big|\psi_m^R\big\rangle \tag{19a}$$

and

$$\tilde{\mathcal{O}}_{m\leftarrow n} = \big\langle\psi_m^L\big|\hat{\mathcal{O}}^\dagger\big|\psi_n^R\big\rangle, \tag{19b}$$

with $\mathcal{O}_{n\leftarrow m} \neq \tilde{\mathcal{O}}^*_{m\leftarrow n}$ when $m \neq n$. For the evaluation of Eq. (18), we require the Hermitian matrix element $\mathcal{O}_{nm}$, which we express in the generic form

$$\mathcal{O}_{nm} = |\mathcal{O}_{nm}| e^{i\phi_{nm}}. \tag{20}$$

To evaluate the modulus of $\mathcal{O}_{nm}$, we adopt the geometric averaging approach proposed by Stanton and Bartlett [65],

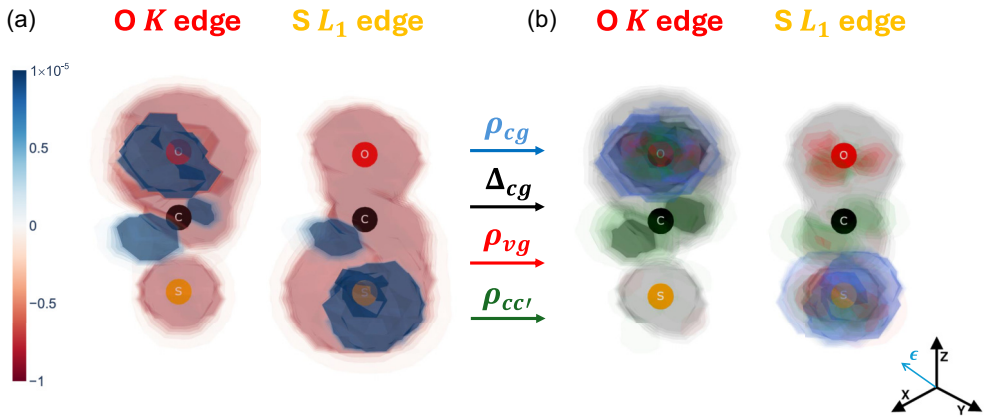


FIG. 2. Difference density $\Delta\rho(\boldsymbol{r},t)$ and its decomposition into density components at 400 as after the peak of the x-ray pulse. (a) Snapshots of $\Delta\rho(\boldsymbol{r},t)$ at 400 as for excitation at the O K edge and S L_1 edge with a pulse polarized at 45° in the xz plane. (b) Visual decomposition of $\Delta\rho(\boldsymbol{r},t)$ in terms of the contributions defined in Eq. (18). The sketch in the lower right corner illustrates the orientation of the axes. The cyan vector shows the orientation of the x-ray polarization vector.

according to which

$$|\mathcal{O}_{nm}| = \sqrt{\mathcal{O}_{n\leftarrow m}\tilde{\mathcal{O}}_{m\leftarrow n}}. \tag{21}$$

We obtain the phase factor appearing in Eq. (20) directly from the phase of the EOM-CC transition matrix element:

$$e^{i\phi_{nm}} = e^{i\phi_{n\leftarrow m}} = \frac{\mathcal{O}_{n\leftarrow m}}{|\mathcal{O}_{n\leftarrow m}|}. \tag{22}$$

We apply this procedure to all the EOM-CC transition properties, i.e., the transition dipole moments, the 1RDMs, and second-order transition moments.

D. Computational details

All the quantum-chemical calculations are performed using a developer version of the Q-CHEM 6.1 software package [78], modified to output both $\gamma_{pq}^{m\leftarrow n}$ and $\gamma_{pq}^{n\leftarrow m}$. The ground-state equilibrium geometries of OCS and oxazole are optimized at the CCSD/aug-cc-pVDZ level of theory (see Appendix A for details). The calculations of the respective electronic structures are performed at the frozen-core (fc), core-valence separation (CVS), EOM, excited-state (EE), coupled-cluster with singles and doubles (CCSD) fc-CVS-EOM-EE-CCSD/6-311 + G* level of theory (see Appendix B for details). For OCS, we include a total of 23 electronic states (ground state, 15 core-excited states, and 7 valence-excited states) in the spectral expansion in Eq. (3); for oxazole, we include a total of 51 electron states (ground state, 30 core-excited states, and 20 valence-excited states). See Appendix C for a detailed description of the energy spectra of OCS and oxazole. We consider a Gaussian pulse (see Appendix D for details) of bandwidth $\Delta\omega = 8$ eV (corresponding to a pulse duration $\Delta t \approx 230$ as), sufficient to coherently populate a large portion of the excited states included in the spectral expansion. Pulses of similar duration and bandwidth in the water window are available at XFEL facilities [21]. We consider a pulse peak intensity $I_0 = 9.1 \times 10^{14}$ W cm^{-2}, which is easily achievable at XFEL facilities and is consistent with the perturbative regime required by the theory. We set the pulse resonant with the $1s \rightarrow \pi^*$ line at the O K edge and S L_1 edge for OCS and at the O K edge and N K edge for oxazole. For both molecules, we assume a fixed relative alignment with respect to the direction of the pulse polarization [83–85].

III. RESULTS

A. Difference density and its decomposition

As a first step, we focus on the analysis of $\Delta\rho(\boldsymbol{r},t)$ and its perturbative decomposition in OCS. In its equilibrium configuration, OCS is linear ($C_{\infty v}$). Since it contains atoms of three different elements, OCS provides energetically well-separated inner-shell edges one can choose for the x-ray excitation.

In Fig. 2(a) we compare $\Delta\rho(\boldsymbol{r},t)$ excited at the O K edge (left) and at the S L_1 edge (right) with a pulse polarized at 45° in the xz plane. In particular, we compare snapshots at 400 as after the peak of the x-ray pulse. At this point in time, the pulse has already begun to fade and the WP formed starts undergoing its dynamical evolution. In both cases, negative-value regions, corresponding to density reduction, are distributed over the whole molecule, whereas positive-value regions, corresponding to density increase, are concentrated mainly at the pumped atom and the neighboring carbon.

To explain this atom-specific distribution of $\Delta\rho(\boldsymbol{r},t)$, we decompose it into the contributions introduced in Eq. (18), as shown in Fig. 2(b). Each component contributes to different regions of $\Delta\rho(\boldsymbol{r},t)$, the contributions of $\rho_{cg}(\boldsymbol{r},t)$ and $\Delta_{cg}(\boldsymbol{r},t)$ generally being larger in magnitude than those coming from $\rho_{cc'}(\boldsymbol{r},t)$ and $\rho_{vg}(\boldsymbol{r},t)$ [86].

The $\rho_{cg}(\boldsymbol{r},t)$ component (blue) corresponds to the polarization in the electronic distribution established in linear response to the interaction with the x-ray pulse. We show the details of its time evolution in Fig. 3(a). At the O K edge (left snapshots), $\rho_{cg}(\boldsymbol{r},t)$ sharply localizes on the oxygen atom and oscillates at a very high frequency proportional to the excitation energy at the O K edge. At the S L_1 edge (right snapshots), $\rho_{cg}(\boldsymbol{r},t)$ localizes on sulfur and oscillates with a longer period than at the O K edge, proportionally to the

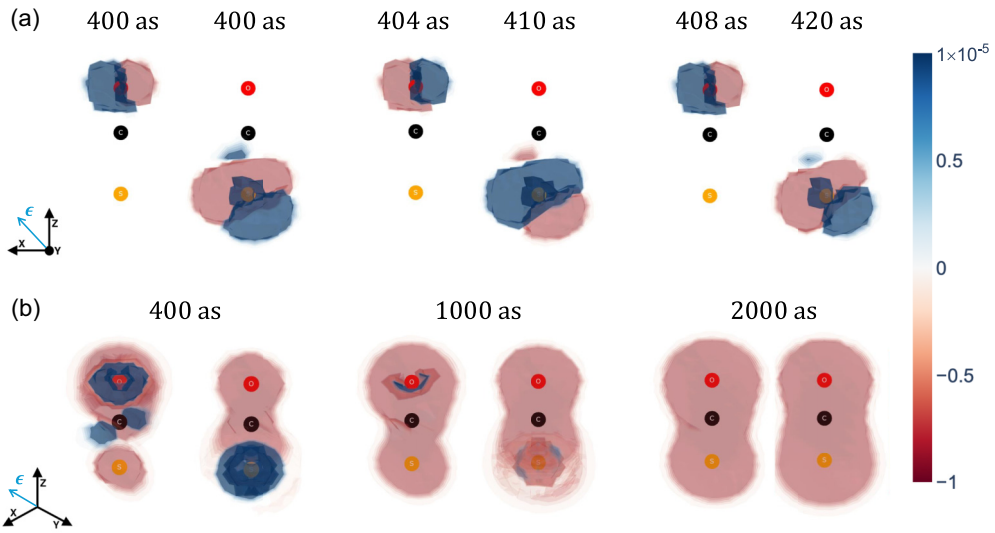


FIG. 3. Time evolution of (a) $\rho_{cg}(\boldsymbol{r}, t)$ and (b) $\Delta_{cg}(\boldsymbol{r}, t)$ for a pulse polarized at 45° in the xz plane. In each panel, the snapshots are ordered in three groups, with time increasing from left to right. The left and right snapshots in each group correspond to the excitation at the O K edge and S L_1 edge, respectively. The sketch in the lower left corner of each panel illustrates the orientation of the axes. The cyan vector corresponds to the orientation of the polarization vector.

lower excitation energies at the S L_1 edge. The atom-specific localization of $\rho_{cg}(\boldsymbol{r}, t)$ shows how the coupling between the x-ray field and the molecule takes place locally on the pumped atom; the linear response induced by the coupling remains localized on the pumped atom and oscillates at the frequency of the resonant transitions involved.

Since $\boldsymbol{\epsilon}$ has components along both the x and z axes, excitations to both Π_x and Σ^+ core-excited states are allowed. The orientation of $\rho_{cg}(\boldsymbol{r}, t)$ in the xz plane reflects the relative contributions from the two types of states. At the O K edge, $\rho_{cg}(\boldsymbol{r}, t)$ oscillates along the x axis, signaling the dominant contribution of excitations to Π_x states. At the S L_1 edge, $\rho_{cg}(\boldsymbol{r}, t)$ is tilted in the xz plane, indicating significant contributions from both Π_x and Σ^+ states.

The $\Delta_{cg}(\boldsymbol{r}, t)$ component corresponds to the difference density obtained by subtracting the (time-independent) ground-state density from the (time-dependent) densities of the core-excited states. In the snapshots from the time evolution of $\Delta_{cg}(\boldsymbol{r}, t)$ shown in Fig. 3(b), the negative-value regions extend over the whole molecule, completely offsetting the positive-value regions as time proceeds. This behavior is caused by the limited lifetime of the core-excited states, which leads to the complete decay of their population within few femtoseconds. The positive-value regions at 400 as, before significant decay has taken place, reflect the population of valence-type orbitals by the core-excited electron. At the O K edge (left), the distribution resembles a π^* orbital extending over the carbon and the oxygen; this shows how the x-ray excitation can be described as a $1s \rightarrow \pi^*$ excitation. This is not the case at the S L_1 edge, where the x-ray excitation involves both Π_x and Σ^+ states. As shown in the right snapshot at 400 as, the positive-value region resides practically exclusively on sulfur, demonstrating a substantially local character of the excitation.

The $\rho_{cc'}(\boldsymbol{r}, t)$ component corresponds to the coherences established between the core-excited states. Since the energy separation between core-excited states is only between 1 and 10 eV, the coherences associated with $\rho_{cc'}(\boldsymbol{r}, t)$ oscillate with periods ranging between hundreds of attoseconds and a few femtoseconds. The oscillation periods of the coherences translate directly to the timescale of the electron-density oscillations within $\rho_{cc'}(\boldsymbol{r}, t)$. As shown in Fig. 2(b), $\rho_{cc'}(\boldsymbol{r}, t)$ provides an initial contribution to $\Delta\rho(\boldsymbol{r}, t)$, although to a lesser extent compared to $\rho_{cg}(\boldsymbol{r}, t)$ and $\Delta_{cg}(\boldsymbol{r}, t)$. Moreover, its effect on $\Delta\rho(\boldsymbol{r}, t)$ quickly fades away due to the fast decay of the core-excited states and is therefore not considered further in this work.

The $\rho_{vg}(\boldsymbol{r}, t)$ component shown in Fig. 2(b) corresponds to the coherences established between the ground state and the valence-excited states via the ISXRS process. Its contribution is comparable to that of $\rho_{cc'}(\boldsymbol{r}, t)$ in the initial stages of the excitation. However, owing to the much longer lifetime of the valence-excited states compared to the core-excited states [75], $\rho_{vg}(\boldsymbol{r}, t)$ decays at a much slower rate than the other components. As time progresses and the core-excited components decay, $\rho_{vg}(\boldsymbol{r}, t)$ gradually becomes the main contribution to $\Delta\rho(\boldsymbol{r}, t)$ (in addition to the stationary contribution from ground-state depopulation). Therefore, on timescales longer than the core-hole lifetime, charge migration within the molecule is captured by $\rho_{vg}(\boldsymbol{r}, t)$. In the next subsection we analyze in detail the electron dynamics within $\rho_{vg}(\boldsymbol{r}, t)$, focusing, in particular, on the role of the x-ray polarization.

B. Charge migration in OCS

The preparation of $\rho_{vg}(\boldsymbol{r}, t)$ and the control over the associated charge migration relies on the tailored combination of molecular and pulse properties via the ISXRS process. In fact, based on the properties of the molecule, i.e., its energy spectrum and the dipole moments between its states, one can use the characteristics of the x-ray pulse (such as its bandwidth,

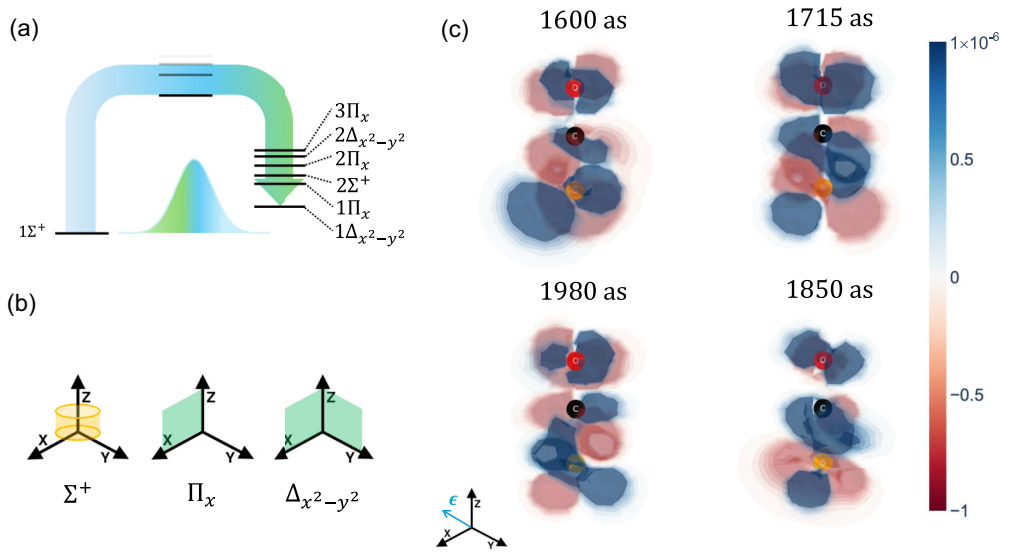


FIG. 4. Properties of a valence-electronic wave packet excited by ISXRS at the S L_1 edge with an x-ray pulse polarized at 45° in the xz plane. (a) Illustration of ISXRS excitation of OCS with a broadband x-ray pulse. (b) Spatial symmetry of the Σ^+, Π_x, and $\Delta_{x^2-y^2}$ valence-excited states. The yellow cylinder represents the cylindrical symmetry of the Σ^+, while the green areas indicate the symmetry planes characterizing the Π_x and $\Delta_{x^2-y^2}$ states. (c) Snapshots illustrating the charge migration by $\rho_{vg}(\boldsymbol{r}, t)$ over a 380-as period [87].

central frequency, and polarization) to control the electronic WP.

In the example presented in Fig. 4, we considered a bandwidth of 8 eV (as already mentioned in Sec. II D) and a polarization at 45° in the xz plane. As shown in Fig. 4(a), these pulse parameters allow us to substantially populate five valence-excited states of Σ^+, Π_x, or $\Delta_{x^2-y^2}$ symmetry. The symmetry of the valence-excited states involved is reflected directly in the spatial distribution of the respective transition densities. In fact, as shown schematically in Fig. 4(b), the Σ^+ states are symmetric with respect to the z axis, the Π_x states are symmetric with respect to xz plane, and the $\Delta_{x^2-y^2}$ states are symmetric with respect to both the xz and the yz planes.

Since the electron dynamics within $\rho_{vg}(\boldsymbol{r}, t)$ originate from the constructive and destructive interference of its coherent components, the spatial distribution of the transition densities directly influences the spatial properties of the charge-migration process, as illustrated in Fig. 4(c). A nodal plane bisecting the CO bond splits the distribution of $\rho_{vg}(\boldsymbol{r}, t)$ in two parts, isolating the electron dynamics around the oxygen from that on the carbon-sulfur moiety. The electron dynamics involving carbon and sulfur is particularly pronounced, as shown in the movie in [87] (whose viewing is highly recommended for a clearer visualization of the dynamics) associated with the snapshots in Fig. 4. Starting from the snapshot at 1600 as, a lump of $\rho_{vg}(\boldsymbol{r}, t)$ accumulates on sulfur on the left side of the yz plane. The charge migration subsequently proceeds towards the right side of the yz plane and then towards the carbon, as shown in the snapshot at 1715 as. As may be seen in the snapshot at 1850 as, the charge migration then changes its direction and proceeds around the carbon towards the left side of the yz plane. Eventually, as shown in the snapshot at 1980 as, the electron density flows back to sulfur on the left side of the yz plane.

The charge migration thus follows a quasicircular path across the yz plane, which breaks the symmetry with respect to the latter and preserves it with respect to the xz plane. This depends directly on the symmetries of the states involved, with all states being symmetric with respect to the xz plane and the Π_x states providing the symmetry breaking that enables the circular migration across the yz plane. This example shows the connection between the symmetry of the states involved in the coherent superposition with the spatial pattern followed by the charge migration. In this context, controlling the relative alignment of the molecule and the (linear) pulse polarization represents a mechanism to influence the spatial pattern of charge migration.

C. Charge migration in oxazole

We applied the decomposition of $\Delta\rho(\boldsymbol{r}, t)$ into its perturbative components also to oxazole. This heterocyclic aromatic molecule contains two heteroatoms, oxygen and nitrogen, and in its equilibrium geometry presents a planar structure of C_s symmetry. Here we study the properties of $\Delta\rho(\boldsymbol{r}, t)$ excited either at the O K edge or at the N K edge. Similarly to OCS, in the initial stages of the time evolution $\rho_{cg}(\boldsymbol{r}, t)$ and $\Delta_{cg}(\boldsymbol{r}, t)$ provide the dominant contributions, their distribution displaying the atom-specific local character of the x-ray excitation. The decay of the core-excited components gives way to $\rho_{vg}(\boldsymbol{r}, t)$, which progressively becomes the main nonstationary contribution to $\Delta\rho(\boldsymbol{r}, t)$.

The spectrum of oxazole includes several low-lying valence-excited states; their symmetry depends on the irreducible representation of the C_s group they belong to: A' states are symmetric upon reflection across the molecular plane (the xy plane in Fig. 5), while A'' states are antisymmetric. Using a pulse polarized at 45° in the xz plane, both

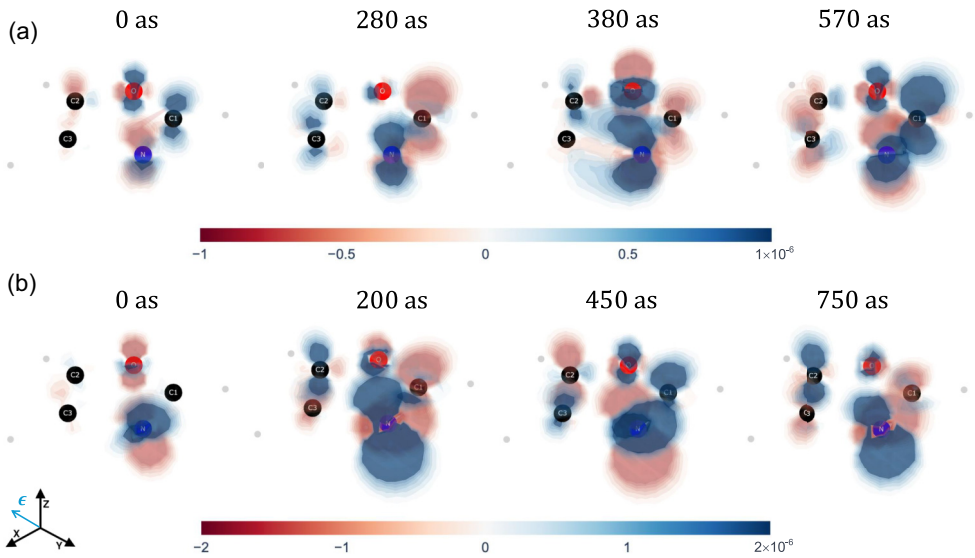


FIG. 5. Atom-specific charge migration in oxazole, as captured by $\rho_{vg}(\boldsymbol{r}, t)$, following the excitation with an x-ray pulse polarized at 45° in the xz plane. (a) Excitation at the O K edge. (b) Excitation at the N K edge. The sketch in the lower left corner shows the orientation of the axes. The cyan vector corresponds to the orientation of the polarization vector [87].

A' and A'' states can be populated. In our case, using a pulse with an 8-eV bandwidth, we can substantially populate 20 valence-excited states (divided equally between the A' and A'' symmetries) within the coherent superposition. Similarly to the example in OCS, including many states of different symmetries enables complex interference patterns between the corresponding coherent components, which in turn support rich electron dynamics. We present an example of the electronic dynamics corresponding to $\rho_{vg}(\boldsymbol{r}, t)$ in Fig. 5, where we compare an excitation at the O K edge [Fig. 5(a)] and at the N K edge [Fig. 5(b)].

The intensity buildup of the pulse corresponds to the preparation phase of $\rho_{vg}(\boldsymbol{r}, t)$, during which its magnitude grows linearly and the electronic motion is frozen [88]. As the pulse gradually fades, the buildup of the coherence terminates and the electronic system evolves freely. As a first step, we analyze the electronic distribution at 0 as, which corresponds to the maximum pulse intensity and the peak of the WP preparation. At this point in time, we can observe the atom-specific effects of the ISXRS excitation on the starting point of the charge migration. As shown in previous works [34,35,64], the atom-specific response to an ISXRS excitation is encoded in the relative amplitudes and phases of the coherent components of $\rho_{vg}(\boldsymbol{r}, t)$. In our example, the atomic specificity is reflected directly in the initial distribution of $\rho_{vg}(\boldsymbol{r}, t)$. In fact, when the molecule is excited at the O K edge [Fig. 5(a)] the density accumulates predominantly on the oxygen and C1, whereas when the molecule is excited at the N K edge [Fig. 5(b)], the density accumulates mainly on the nitrogen. This shows how the ISXRS process can be used to control the starting point of charge migration, which can be chosen by tuning the x-ray pulse to a specific inner-shell edge of the molecule.

Departing from the edge-dependent initial configuration, the charge migration initially unfolds in a clockwise direction. This can be seen by observing the density increase or decrease on C1, C2, and C3 in the snapshots in Fig. 5 (we highly recommend watching the movies associated with Fig. 5 [87] for a clearer visualization of the dynamics). At the O K edge [Fig. 5(a)], the migration starts from O and C1 at 0 as, moves clockwise through N and C3 at 280 as, reaches C2 at 380 as, and returns to C1 at 570 as. At the N K edge [Fig. 5(b)], starting from N at 0 as the charge migration reaches C2 at 200 as, quickly passes through C1 and C3 at 450 as, and eventually returns to C2 at 750 as. Following the first few hundred attoseconds [87], the subsequent electron dynamics behaves similarly to clockwise and counterclockwise ring currents, as is typical for heteroaromatic systems of this type [89–93]. None of the directions prevails, with the two modes alternating (in a pattern characteristic of the chosen x-ray excitation edge) and the electron dynamics often being limited to oscillations between pairs of atoms.

Similarly to the OCS example, mixing states of A' and A'' symmetry enables the charge migration to break through the symmetry plane of the molecule. This is not particularly evident at the O K edge [Fig. 5(a)], where the A' states are predominantly populated. However, at the N K edge [Fig. 5(b)], owing to a comparable population of A' and A'' states, the charge migration proceeds also across the xy plane. This is particularly evident on the N atom, where the (positive- and negative-value) density lobes undergo a circular motion across the xy plane.

IV. CONCLUSION

In this work we presented a perturbative framework for computing the dynamics of an electronic WP launched by an intense, broadband x-ray pulse in a neutral molecule. We coherently populated both the core-excited states and the valence-excited states by considering a linear x-ray absorption and a nonlinear ISXRS process as excitation mechanisms. We described the electronic structure and its properties at the EOM-CC level of theory, adopting an accurate

implementation that avoids the truncation of the sum over states characterizing the RIXS transition moments. This provides an accurate description of the ISXRS process, improving on the commonly used truncation in the evaluation of the RIXS moments.

We studied the excitation and dynamics of an electronic WP within OCS and oxazole, by monitoring the evolution of the time-dependent difference electron density. We separated the contributions of the excitation mechanisms by decomposing the time-dependent difference electron density into its perturbative components. We observed that the density components associated with core-excited states provide the main contributions to the difference density during the first few femtoseconds of the electronic dynamics. Their spatial distribution gives a visual representation of the atomic specificity and local character of the x-ray excitation. The relative contribution of the components changes with time: While the population of the core-excited states decays within a few femtoseconds, the relative contribution of the valence-excited component progressively becomes the dominant nonstationary one. The coherent population of the valence-excited states via ISXRS provides a longer-lived platform for charge migration compared to the core-excited states.

We focused more in depth on the valence-electron dynamics by studying the effect of the x-ray pulse parameters on the WP launched via ISXRS. In both OCS and oxazole, we showed how the symmetry of the states included in the quantum superposition shapes the spatial pattern followed by charge migration. Accordingly, controlling the relative orientation of the molecule and the pulse polarization represents a tool to influence charge migration and its spatial properties. In oxazole, we showed how the atom specificity of ISXRS is reflected in the initial distribution of the electron density. This shows the capability of ISXRS to spatially control the starting point of charge migration by tuning the x-ray pulse to a specific inner-shell edge of the molecule. We examined the characteristics of the subsequent charge migration, showing how it unfolds according to a well-known pattern of clockwise and counterclockwise ring currents.

While being limited in the range of available pulse intensities, the perturbative framework presented in this work allows an accurate description of the molecular electronic structure and a flexible selection of the properties of the pulse and the one-particle observable. This enables future studies exploring the influence of the pulse properties on the electronic dynamics (e.g., by considering realistic SASE pulses produced by an XFEL or amplitude- and phase-optimized x-ray pulses) and the extent of coherent control possible in both ideal and experimentally realistic conditions. The framework can also be readily adapted to the simulation of ultrafast pump-probe experiments by considering spectroscopic one-particle observables.

In this paper we studied purely coherent electron dynamics without considering the decoherence effects associated with the nuclear degrees of freedom [94–96]. Given the absence of hydrogen atoms in OCS, we do not expect that the inclusion of ground-state structural fluctuations would lead to considerable modifications of the electron dynamics in OCS that we have predicted. In oxazole, structural quantum fluctuations are more likely to have an impact on electronic coherence, but not so much on the subfemtosecond timescale we considered in Fig. 5. Nevertheless, an important future extension of this work would entail including such effects in the theoretical framework. This would provide a more complete picture of the excitation, the intramolecular electron dynamics, and their dependence on the x-ray pulse parameters, while extending the capabilities of the framework towards fully predictive calculations of attosecond-pulse-induced chemical dynamics.

TABLE I. Equilibrium geometry of OCS ($E_{\text{nuc}} = 78.390$ Ha).

Atom	x (Å)	y (Å)	z (Å)
S	0.000	0.000	–1.052
C	0.000	0.000	0.537
O	0.000	0.000	1.701

ACKNOWLEDGMENTS

We thank Dr. Mads Pedersen for his help with the computational implementation. This work was supported by the Cluster of Excellence CUI: Advanced Imaging of Matter of the Deutsche Forschungsgemeinschaft, EXC 2056, Project No. 390715994. E.R., S.C., N.R., and R.S. acknowledge support from DESY (Hamburg, Germany), a member of the Helmholtz Association HGF. The work at USC was supported by the U.S. National Science Foundation (Grant No. CHE-2525964). A.I.K. also acknowledges support from the Mildred Dresselhaus Guest Professorship during her sabbatical stay at DESY.

DATA AVAILABILITY

The movies supporting the findings of this study are available from [87] .

APPENDIX A: OPTIMIZED NUCLEAR GEOMETRIES

The equilibrium geometries of OCS and oxazole are provided in Tables I and II, respectively.

APPENDIX B: QUANTUM-CHEMICAL CALCULATION PROTOCOL

The electronic-structure calculation follows a three-step protocol: A restricted Hartree-Fock (HF) calculation precedes a ground-state CCSD calculation, with the final step being

TABLE II. Equilibrium geometry of oxazole ($E_{\text{nuc}} = 161.949$ Ha).

Atom	x (Å)	y (Å)	z (Å)
O	–0.360	–1.096	0.000
C	–1.105	0.047	0.000
H	–2.185	–0.074	0.000
N	–0.422	1.154	0.000
C	0.944	–0.644	0.000
H	1.726	–1.397	0.000
C	0.918	0.720	0.000
H	1.750	1.420	0.000

TABLE III. Excitation energies of valence-excited states of OCS.

$\|\psi_v\rangle$	ω_{vg} (eV)
$1\Delta_{x^2-y^2}$	5.75
$1\Pi_x$	7.21
$2\Sigma^+$	8.22
$2\Pi_x$	8.43
$2\Delta_{x^2-y^2}$	9.10
$3\Pi_x$	9.18

an fc-CVS-EOM-EE-CCSD calculation. In order to assemble the time-dependent electron density correctly, it is necessary to obtain all the necessary quantities from a single calculation. This is needed since each HF molecular orbital and EOM-CC state is determined only up to a sign, which may in principle change between different instances of the same calculation unless phase is fixed by a convention. Assembling the electron density using the output of a single calculation instance ensures a consistent treatment of the signs and the reproducibility of the results.

APPENDIX C: ENERGY SPECTRA

1. Energy spectrum of OCS

The transition energies relative to the ground state $1\Sigma^+$ for the considered valence-excited states are shown in Table III. The states are labeled according to the irreducible representations of the $C_{\infty v}$ group. The transition energies relative to the ground state $1\Sigma^+$ for the considered core-excited states are shown in Table IV. The ω_{cg}^{S} columns correspond to the excitation energies at the S $L1$ edge and the ω_{cg}^{O} columns correspond to the excitation energies at the O K edge. The values highlighted in bold correspond to the calculated energies for the $1s \rightarrow \pi^*$ transition.

2. Energy spectrum of oxazole

The transition energies relative to the ground state $1A'$ for the considered valence-excited states are shown in Table V. The states are labeled according to the irreducible representations of the C_s group. The transition energies relative to the ground state $1A'$ for the considered core-excited states are shown in Table VI. The ω_{cg}^{N} columns correspond to the excitation energies at the N K edge and the ω_{cg}^{O} columns correspond to the excitation energies at the O K edge. The values highlighted in bold correspond to the calculated energies for the $1s \rightarrow \pi^*$ transition.

TABLE IV. Excitation energies of core-excited states of OCS.

$\|\psi_c\rangle$	ω_{cg}^{S} (eV)	ω_{cg}^{O} (eV)	$\|\psi_c\rangle$	ω_{cg}^{S} (eV)	ω_{cg}^{O} (eV)
$1\,^c\Sigma^+$	230.74	538.50	$1\,^c\Pi_x$, $1\,^c\Pi_y$	**229.74**	**535.63**
$2\,^c\Sigma^+$	232.07	540.61	$2\,^c\Pi_x$, $2\,^c\Pi_y$	233.50	540.84
$3\,^c\Sigma^+$	232.42	541.32	$3\,^c\Pi_x$, $3\,^c\Pi_y$	234.98	542.42
$4\,^c\Sigma^+$	235.00	541.89	$4\,^c\Pi_x$, $4\,^c\Pi_y$	239.75	545.63
$5\,^c\Sigma^+$	236.54	543.97	$5\,^c\Pi_x$, $5\,^c\Pi_y$	240.48	549.20

TABLE V. Excitation energies of valence-excited states of oxazole.

$\|\psi_v\rangle$	ω_{vg} (eV)	$\|\psi_v\rangle$	ω_{vg} (eV)
$2A'$	6.76	$1A''$	6.78
$3A'$	7.42	$2A''$	6.97
$4A'$	8.18	$3A''$	7.57
$5A'$	8.31	$4A''$	7.90
$6A'$	8.80	$5A''$	8.06
$7A'$	8.99	$6A''$	8.41
$8A'$	9.23	$7A''$	8.57
$9A'$	9.33	$8A''$	8.76
$10A'$	9.48	$9A''$	8.82
$11A'$	9.68	$10A''$	9.45

APPENDIX D: DESCRIPTION OF THE LIGHT PULSE

We define $E(\omega)$ as the Fourier transform of the Gaussian pulse

$$E(t) = E_0 e^{-\beta t^2} \cos(\omega_f t), \tag{D1}$$

where ω_f is the carrier frequency, while β is related to the pulse bandwidth $\Delta\nu$ and duration Δt as

$$\Delta\nu = \frac{\Delta\omega}{2\pi} = \frac{\sqrt{2\beta \ln 2}}{\pi}, \quad \Delta t = \sqrt{\frac{2\ln 2}{\beta}}, \tag{D2}$$

respectively. In SI units, the peak intensity resulting from Eq. (D1) is given by

$$I_0 = \tfrac{1}{2} c \epsilon_0 E_0^2, \tag{D3}$$

where c is the speed of light and ϵ_0 is the vacuum permittivity.

TABLE VI. Excitation energies of core-excited states of oxazole.

$\|\psi_c\rangle$	ω_{cg}^{N} (eV)	ω_{cg}^{O} (eV)	$\|\psi_c\rangle$	ω_{cg}^{N} (eV)	ω_{cg}^{O} (eV)
$1\,^cA'$	403.99	539.16	$1\,^cA''$	**400.87**	**536.99**
$2\,^cA'$	404.73	540.10	$2\,^cA''$	403.83	540.32
$3\,^cA'$	404.97	540.29	$3\,^cA''$	405.13	540.79
$4\,^cA'$	405.01	540.67	$4\,^cA''$	406.34	541.98
$5\,^cA'$	405.49	540.99	$5\,^cA''$	406.97	542.66
$6\,^cA'$	405.88	541.34	$6\,^cA''$	408.90	545.07
$7\,^cA'$	407.08	542.17	$7\,^cA''$	410.95	545.74
$8\,^cA'$	407.29	542.73	$8\,^cA''$	417.32	554.12
$9\,^cA'$	407.71	542.82	$9\,^cA''$	418.02	554.36
$10\,^cA'$	408.33	543.46	$10\,^cA''$	418.93	556.28
$11\,^cA'$	408.51	543.96	$11\,^cA''$	419.58	556.54
$12\,^cA'$	408.65	544.58	$12\,^cA''$	420.49	559.63
$13\,^cA'$	409.00	544.76	$13\,^cA''$	422.00	560.78
$14\,^cA'$	409.57	545.04	$14\,^cA''$	422.39	560.99
$15\,^cA'$	409.99	545.88	$15\,^cA''$	423.52	561.15

[1] A. H. Zewail, Femtochemistry: Atomic-scale dynamics of the chemical bond, J. Phys. Chem. A **104**, 5660 (2000).

[2] X. Hu, K. F. Mak, J. Zhang, Z. Wei, and F. Krausz, Ultrafast lasers for attosecond science, Light: Sci. Appl. **15**, 24 (2026).

[3] P. M. Paul, E. S. Toma, P. Breger, G. Mullot, F. Augé, P. Balcou, H. G. Muller, and P. Agostini, Observation of a train of attosecond pulses from high harmonic generation, Science **292**, 1689 (2001).

[4] F. Remacle and R. D. Levine, An electronic time scale in chemistry, Proc. Natl. Acad. Sci. USA **103**, 6793 (2006).

[5] F. Lépine, M. Y. Ivanov, and M. J. J. Vrakking, Attosecond molecular dynamics: Fact or fiction? Nat. Photonics **8**, 195 (2014).

[6] K.-M. Weitzel, Controlling the electrons provides means for controlling chemistry, ChemPhysChem **8**, 213 (2007).

[7] F. Remacle, R. D. Levine, and M. S. Ratner, Charge directed reactivity: A simple electronic model, exhibiting site selectivity, for the dissociation of ions, Chem. Phys. Lett. **285**, 25 (1998).

[8] F. Remacle, R. D. Levine, E. W. Schlag, and R. Weinkauf, Electronic control of site selective reactivity: A model combining charge migration and dissociation, J. Phys. Chem. A **103**, 10149 (1999).

[9] A. I. Kuleff and L. S. Cederbaum, Ultrafast correlation-driven electron dynamics, J. Phys. B: At. Mol. Opt. Phys. **47**, 124002 (2014).

[10] I. C. D. Merritt, D. Jacquemin, and M. Vacher, Attochemistry: Is controlling electrons the future of photochemistry? J. Phys. Chem. Lett. **12**, 8404 (2021).

[11] L. Cederbaum and J. Zobeley, Ultrafast charge migration by electron correlation, Chem. Phys. Lett. **307**, 205 (1999).

[12] H. J. Wörner, C. A. Arrell, N. Banerji, A. Cannizzo, M. Chergui, A. K. Das, P. Hamm, U. Keller, P. M. Kraus, E. Liberatore, P. Lopez-Tarifa, M. Lucchini, M. Meuwly, C. Milne, J.-E. Moser, U. Rothlisberger, G. Smolentsev, J. Teuscher, J. A. van Bokhoven, and O. Wenger, Charge migration and charge transfer in molecular systems, Struct. Dyn. **4**, 061508 (2017).

[13] F. Calegari, D. Ayuso, A. Trabattoni, L. Belshaw, S. De Camillis, S. Anumula, F. Frassetto, L. Poletto, A. Palacios, P. Decleva, J. B. Greenwood, F. Martín, and M. Nisoli, Ultrafast electron dynamics in phenylalanine initiated by attosecond pulses, Science **346**, 336 (2014).

[14] P. M. Kraus, B. Mignolet, D. Baykusheva, A. Rupenyan, L. Horný, E. F. Penka, G. Grassi, O. I. Tolstikhin, J. Schneider, F. Jensen, L. B. Madsen, A. D. Bandrauk, F. Remacle, and H. J. Wörner, Measurement and laser control of attosecond charge migration in ionized iodoacetylene, Science **350**, 790 (2015).

[15] A. S. Folorunso, F. Mauger, K. A. Hamer, D. D. Jayasinghe, I. S. Wahyutama, J. R. Ragains, R. R. Jones, L. F. DiMauro, M. B. Gaarde, K. J. Schafer, and K. Lopata, Attochemistry regulation of charge migration, J. Phys. Chem. A **127**, 1894 (2023).

[16] L. Fransén, S. Gómez, and M. Vacher, Attochemical control of nuclear motion despite fast electronic decoherence, J. Phys. Chem. Lett. **16**, 8745 (2025).

[17] N. V. Golubev and A. I. Kuleff, Control of charge migration in molecules by ultrashort laser pulses, Phys. Rev. A **91**, 051401(R) (2015).

[18] K. Glusac, What has light ever done for chemistry? Nat. Chem. **8**, 734 (2016).

[19] D. T. Matselyukh, V. Despré, N. V. Golubev, A. I. Kuleff, and H. J. Wörner, Decoherence and revival in attosecond charge migration driven by non-adiabatic dynamics, Nat. Phys. **18**, 1206 (2022).

[20] F. Calegari and F. Martin, Open questions in attochemistry, Commun. Chem. **6**, 184 (2023).

[21] J. Duris, S. Li, T. Driver, E. G. Champenois, J. P. MacArthur, A. A. Lutman, Z. Zhang, P. Rosenberger, J. W. Aldrich, R. Coffee, G. Coslovich, F.-J. Decker, J. M. Glownia, G. Hartmann, W. Helml, A. Kamalov, J. Knurr, J. Krzywinski, M.-F. Lin, J. P. Marangos, *et al.*, Tunable isolated attosecond X-ray pulses with gigawatt peak power from a free-electron laser, Nat. Photonics **14**, 30 (2020).

[22] J. Stöhr, *NEXAFS Spectroscopy* (Springer, Berlin, 2010).

[23] S. Tanaka and S. Mukamel, Coherent x-ray Raman spectroscopy: A nonlinear local probe for electronic excitations, Phys. Rev. Lett. **89**, 043001 (2002).

[24] U. Harbola and S. Mukamel, Coherent stimulated x-ray Raman spectroscopy: Attosecond extension of resonant inelastic x-ray Raman scattering, Phys. Rev. B **79**, 085108 (2009).

[25] J. D. Biggs, Y. Zhang, D. Healion, and S. Mukamel, Two-dimensional stimulated resonance Raman spectroscopy of molecules with broadband x-ray pulses, J. Chem. Phys. **136**, 174117 (2012).

[26] N. Rohringer, X-ray Raman scattering: A building block for nonlinear spectroscopy, Philos. Trans. R. Soc. A **377**, 20170471 (2019).

[27] C. Weninger, M. Purvis, D. Ryan, R. A. London, J. D. Bozek, C. Bostedt, A. Graf, G. Brown, J. J. Rocca, and N. Rohringer, Stimulated electronic x-ray Raman scattering, Phys. Rev. Lett. **111**, 233902 (2013).

[28] V. Kimberg, A. Sanchez-Gonzalez, L. Mercadier, C. Weninger, A. Lutman, D. Ratner, R. Coffee, M. Bucher, M. Mucke, M. Agåker, C. Såthe, C. Bostedt, J. Nordgren, J. E. Rubensson, and N. Rohringer, Stimulated x-ray Raman scattering – a critical assessment of the building block of nonlinear x-ray spectroscopy, Faraday Discuss. **194**, 305 (2016).

[29] J. T. O'Neal, E. G. Champenois, S. Oberli, R. Obaid, A. Al-Haddad, J. Barnard, N. Berrah, R. Coffee, J. Duris, G. Galinis, D. Garratt, J. M. Glownia, D. Haxton, P. Ho, S. Li, X. Li, J. MacArthur, J. P. Marangos, A. Natan, N. Shivaram, *et al.*, Electronic population transfer via impulsive stimulated x-ray Raman scattering with attosecond soft-x-ray pulses, Phys. Rev. Lett. **125**, 073203 (2020).

[30] O. Alexander, F. Egun, L. Rego, A. M. Gutierrez, D. Garratt, G. A. Cárdenas, J. J. Nogueira, J. P. Lee, K. Zhao, R.-P. Wang, D. Ayuso, J. C. T. Barnard, S. Beauvarlet, P. H. Bucksbaum, D. Cesar, R. Coffee, J. Duris, L. J. Frasinski, N. Huse, K. M. Kowalczyk, *et al.*, Attosecond impulsive stimulated X-ray Raman scattering in liquid water, Sci. Adv. **10**, eadp0841 (2024).

[31] K. Li, C. Ott, M. Agåker, P. J. Ho, G. Doumy, A. Magunia, M. Rebholz, M. Simon, T. Mazza, A. De Fanis, T. M. Baumann, J. Montano, N. Rennhack, S. Usenko, Y. Ovcharenko, K. Chordiya, L. Cheng, J.-E. Rubensson, M. Meyer, T. Pfeifer, *et al.*, Super-resolution stimulated x-ray Raman spectroscopy, Nature (London) **643**, 662 (2025).

[32] I. V. Schweigert and S. Mukamel, Probing valence electronic wave-packet dynamics by all x-ray stimulated Raman spectroscopy: A simulation study, Phys. Rev. A **76**, 012504 (2007).

[33] D. Healion, Y. Zhang, J. D. Biggs, N. Govind, and S. Mukamel, Entangled valence electron–hole dynamics revealed by stimulated attosecond x-ray Raman scattering, J. Phys. Chem. Lett. **3**, 2326 (2012).

[34] H. Yong, S. M. Cavaletto, and S. Mukamel, Ultrafast valence-electron dynamics in oxazole monitored by x-ray diffraction following a stimulated X-ray Raman excitation, J. Phys. Chem. Lett. **12**, 9800 (2021).

[35] A. E. A. Fouda and P. J. Ho, Site-specific generation of excited state wavepackets with high-intensity attosecond x rays, J. Chem. Phys. **154**, 224111 (2021).

[36] E. Runge and E. K. U. Gross, Density-functional theory for time-dependent systems, Phys. Rev. Lett. **52**, 997 (1984).

[37] V. Véniard, R. Taïeb, and A. Maquet, Atomic clusters submitted to an intense short laser pulse: A density-functional approach, Phys. Rev. A **65**, 013202 (2001).

[38] A. Bruner, S. Hernandez, F. Mauger, P. M. Abanador, D. J. LaMaster, M. B. Gaarde, K. J. Schafer, and K. Lopata, Attosecond charge migration with TDDFT: Accurate dynamics from a well-defined initial state, J. Phys. Chem. Lett. **8**, 3991 (2017).

[39] L. Greenman, P. J. Ho, S. Pabst, E. Kamarchik, D. A. Mazziotti, and R. Santra, Implementation of the time-dependent configuration-interaction singles method for atomic strong-field processes, Phys. Rev. A **82**, 023406 (2010).

[40] S. Carlström, M. Spanner, and S. Patchkovskii, General time-dependent configuration-interaction singles. I. Molecular case, Phys. Rev. A **106**, 043104 (2022).

[41] T. Klamroth, Optimal control of ultrafast laser driven many-electron dynamics in a polyatomic molecule: *N*-methyl-6-quinolone, J. Chem. Phys. **124**, 144310 (2006).

[42] I. S. Ulusoy, Z. Stewart, and A. K. Wilson, The role of the CI expansion length in time-dependent studies, J. Chem. Phys. **148**, 014107 (2018).

[43] P. Krause, T. Klamroth, and P. Saalfrank, Molecular response properties from explicitly time-dependent configuration interaction methods, J. Chem. Phys. **127**, 034107 (2007).

[44] P. Krause, T. Klamroth, and P. Saalfrank, Time-dependent configuration-interaction calculations of laser-pulse-driven many-electron dynamics: Controlled dipole switching in lithium cyanide, J. Chem. Phys. **123**, 074105 (2005).

[45] H.-D. Meyer, U. Manthe, and L. Cederbaum, The multi-configurational time-dependent Hartree approach, Chem. Phys. Lett. **165**, 73 (1990).

[46] A. U. J. Lode, C. Lévêque, L. B. Madsen, A. I. Streltsov, and O. E. Alon, *Colloquium*: Multiconfigurational time-dependent Hartree approaches for indistinguishable particles, Rev. Mod. Phys. **92**, 011001 (2020).

[47] J. Caillat, J. Zanghellini, M. Kitzler, O. Koch, W. Kreuzer, and A. Scrinzi, Correlated multielectron systems in strong laser fields: A multiconfiguration time-dependent Hartree-Fock approach, Phys. Rev. A **71**, 012712 (2005).

[48] D. Hochstuhl, C. Hinz, and M. Bonitz, Time-dependent multiconfiguration methods for the numerical simulation of photoionization processes of many-electron atoms, Eur. Phys. J.: Spec. Top. **223**, 177 (2014).

[49] K. C. Kulander, Time-dependent Hartree-Fock theory of multiphoton ionization: Helium, Phys. Rev. A **36**, 2726 (1987).

[50] T. Sato and K. L. Ishikawa, Time-dependent complete-active-space self-consistent-field method for multielectron dynamics in intense laser fields, Phys. Rev. A **88**, 023402 (2013).

[51] H. Miyagi and L. B. Madsen, Time-dependent restricted-active-space self-consistent-field theory with space partition, Phys. Rev. A **95**, 023415 (2017).

[52] T. Kato and H. Kono, Time-dependent multiconfiguration theory for electronic dynamics of molecules in an intense laser field, Chem. Phys. Lett. **392**, 533 (2004).

[53] A. Dreuw and M. Wormit, The algebraic diagrammatic construction scheme for the polarization propagator for the calculation of excited states, WIREs Comput. Mol. Sci. **5**, 82 (2015).

[54] A. I. Kuleff, J. Breidbach, and L. S. Cederbaum, Multielectron wave-packet propagation: General theory and application, J. Chem. Phys. **123**, 044111 (2005).

[55] M. Ruberti, P. Decleva, and V. Averbukh, Full *ab initio* many-electron simulation of attosecond molecular pump–probe spectroscopy, J. Chem. Theory Comput. **14**, 4991 (2018).

[56] H. Koch and P. Jørgensen, Coupled cluster response functions, J. Chem. Phys. **93**, 3333 (1990).

[57] A. S. Skeidsvoll, A. Balbi, and H. Koch, Time-dependent coupled-cluster theory for ultrafast transient-absorption spectroscopy, Phys. Rev. A **102**, 023115 (2020).

[58] S. Kvaal, *Ab initio* quantum dynamics using coupled-cluster, J. Chem. Phys. **136**, 194109 (2012).

[59] T. Sato, H. Pathak, Y. Orimo, and K. L. Ishikawa, Communication: Time-dependent optimized coupled-cluster method for multielectron dynamics, J. Chem. Phys. **148**, 051101 (2018).

[60] H. Pathak, T. Sato, and K. L. Ishikawa, Time-dependent optimized coupled-cluster method for multielectron dynamics. IV. Approximate consideration of the triple excitation amplitudes, J. Chem. Phys. **154**, 234104 (2021).

[61] J. A. Sonk, M. Caricato, and H. B. Schlegel, TD-CI simulation of the electronic optical response of molecules in intense fields: Comparison of RPA, CIS, CIS(D), and EOM-CCSD, J. Phys. Chem. A **115**, 4678 (2011).

[62] E. Luppi and M. Head-Gordon, Computation of high-harmonic generation spectra of H_2 and N_2 in intense laser pulses using quantum chemistry methods and time-dependent density functional theory, Mol. Phys. **110**, 909 (2012).

[63] A. S. Skeidsvoll, T. Moitra, A. Balbi, A. C. Paul, S. Coriani, and H. Koch, Simulating weak-field attosecond processes with a Lanczos reduced basis approach to time-dependent equation-of-motion coupled-cluster theory, Phys. Rev. A **105**, 023103 (2022).

[64] A. Balbi, A. S. Skeidsvoll, and H. Koch, Coupled cluster simulation of impulsive stimulated x-ray Raman scattering, J. Phys. Chem. A **127**, 8676 (2023).

[65] J. F. Stanton and R. J. Bartlett, The equation of motion coupled-cluster method. A systematic biorthogonal approach to molecular excitation energies, transition probabilities, and excited state properties, J. Chem. Phys. **98**, 7029 (1993).

[66] A. I. Krylov, Equation-of-motion coupled-cluster methods for open-shell and electronically excited species: The hitchhiker's guide to Fock space, Annu. Rev. Phys. Chem. **59**, 433 (2008).

[67] T. Fransson, I. E. Brumboiu, M. L. Vidal, P. Norman, S. Coriani, and A. Dreuw, XABOOM: An x-ray absorption benchmark of organic molecules based on carbon, nitrogen, and oxygen 1s $\rightarrow$ π^* transitions, J. Chem. Theory Comput. **17**, 1618 (2021).

[68] D. Maganas, P. Kristiansen, L.-C. Duda, A. Knop-Gericke, S. DeBeer, R. Schlögl, and F. Neese, Combined experimental and

ab initio multireference configuration interaction study of the resonant inelastic x-ray scattering spectrum of CO_2, J. Phys. Chem. C **118**, 20163 (2014).

[69] E. Ertan, V. Savchenko, N. Ignatova, V. Vaz da Cruz, R. C. Couto, S. Eckert, M. Fondell, M. Dantz, B. Kennedy, T. Schmitt, A. Pietzsch, A. Föhlisch, F. Gel'mukhanov, M. Odelius, and V. Kimberg, Ultrafast dissociation features in RIXS spectra of the water molecule, Phys. Chem. Chem. Phys. **20**, 14384 (2018).

[70] K. D. Nanda, M. L. Vidal, R. Faber, S. Coriani, and A. I. Krylov, How to stay out of trouble in RIXS calculations within equation-of-motion coupled-cluster damped response theory? Safe hitchhiking in the excitation manifold by means of core–valence separation, Phys. Chem. Chem. Phys. **22**, 2629 (2020).

[71] A. Szabo and N. S. Ostlund, *Modern Quantum Chemistry: Introduction to Advanced Electronic Structure Theory* (Dover, New York, 1989).

[72] A. Menzel, S. Benzaid, M. O. Krause, C. D. Caldwell, U. Hergenhahn, and M. Bissen, Natural widths in open-shell atoms: The K absorption spectrum of atomic oxygen, Phys. Rev. A **54**, R991(R) (1996).

[73] C. Nicolas and C. Miron, Lifetime broadening of core-excited and -ionized states, J. Electron Spectrosc. Relat. Phenom. **185**, 267 (2012).

[74] P. Pyykkö and M. Atsumi, Molecular double-bond covalent radii for elements Li–E112, Chem.—Eur. J. **15**, 12770 (2009).

[75] N. Boens, W. Qin, N. Basarić, J. Hofkens, M. Ameloot, J. Pouget, J.-P. Lefèvre, B. Valeur, E. Gratton, M. vandeVen, N. D. Silva, Y. Engelborghs, K. Willaert, A. Sillen, G. Rumbles, D. Phillips, A. J. W. G. Visser, A. van Hoek, J. R. Lakowicz, H. Malak, *et al.*, Fluorescence lifetime standards for time and frequency domain fluorescence spectroscopy, Anal. Chem. **79**, 2137 (2007).

[76] H. A. Kramers and W. Heisenberg, Über die streuung von strahlung durch atome, Z. Phys. **31**, 681 (1925).

[77] F. Gel'mukhanov and H. Ågren, Resonant x-ray Raman scattering, Phys. Rep. **312**, 87 (1999).

[78] E. Epifanovsky, A. T. B. Gilbert, X. Feng, J. Lee, Y. Mao, N. Mardirossian, P. Pokhilko, A. F. White, M. P. Coons, A. L. Dempwolff, Z. Gan, D. Hait, P. R. Horn, L. D. Jacobson, I. Kaliman, J. Kussmann, A. W. Lange, K. U. Lao, D. S. Levine, J. Liu, *et al.*, Software for the frontiers of quantum chemistry: An overview of developments in the Q-Chem 5 package, J. Chem. Phys. **155**, 084801 (2021).

[79] R. J. Glauber, The quantum theory of optical coherence, Phys. Rev. **130**, 2529 (1963).

[80] N. Rohringer and R. Santra, X-ray nonlinear optical processes using a self-amplified spontaneous emission free-electron laser, Phys. Rev. A **76**, 033416 (2007).

[81] E. L. Saldin, E. A. Schneidmiller, and M. V. Yurkov, Coherence properties of the radiation from x-ray free electron laser, Opt. Commun. **281**, 1179 (2008).

[82] A. I. Krylov, From orbitals to observables and back, J. Chem. Phys. **153**, 080901 (2020).

[83] H. Stapelfeldt and T. Seideman, *Colloquium*: Aligning molecules with strong laser pulses, Rev. Mod. Phys. **75**, 543 (2003).

[84] M. Di Fraia, P. Finetti, R. Richter, K. C. Prince, J. Wiese, M. Devetta, M. Negro, C. Vozzi, A. G. Ciriolo, A. Pusala, A. Demidovich, M. B. Danailov, E. T. Karamatskos, S. Trippel, J. Küpper, and C. Callegari, Impulsive laser-induced alignment of OCS molecules at FERMI, Phys. Chem. Chem. Phys. **19**, 19733 (2017).

[85] T. Mullins, E. T. Karamatskos, J. Wiese, J. Onvlee, A. Rouzée, A. Yachmenev, S. Trippel, and J. Küpper, Picosecond pulse-shaping for strong three-dimensional field-free alignment of generic asymmetric-top molecules, Nat. Commun. **13**, 1431 (2022).

[86] This corresponds to quantitative differences in the relative magnitudes of the corresponding populations and coherences. In fact, with reference to Eq. (18), $\rho_{cg}^{(1)}(t)$ is of the order 10^{-2}, $\rho_{cc}^{(2)}(t)$ and $\rho_{gg}^{(2)}(t)$ are of the order 10^{-3}, and $\rho_{cc'}^{(2)}(t)$ and $\rho_{vg}^{(2)}(t)$ are of the order 10^{-4}.

[87] E. Rossi, Movies of "Preparation and control of electronic wave packets in neutral molecules via attosecond x-ray processes", Zenodo, 2026, https://doi.org/10.5281/zenodo.20774755.

[88] M. Shapiro and P. Brumer, *Quantum Control of Molecular Processes* (Wiley, New York, 2011), Chap. 1, pp. 1–3.

[89] G. Hermann, C. Liu, J. Manz, B. Paulus, J. F. Pérez-Torres, V. Pohl, and J. C. Tremblay, Multidirectional angular electronic flux during adiabatic attosecond charge migration in excited benzene, J. Phys. Chem. A **120**, 5360 (2016).

[90] D. Jia, J. Manz, B. Paulus, V. Pohl, J. C. Tremblay, and Y. Yang, Quantum control of electronic fluxes during adiabatic attosecond charge migration in degenerate superposition states of benzene, Chem. Phys. **482**, 146 (2017).

[91] H. Mineo, S. H. Lin, and Y. Fujimura, Coherent π-electron dynamics of (P)-2, 2′-biphenol induced by ultrashort linearly polarized UV pulses: Angular momentum and ring current, J. Chem. Phys. **138**, 074304 (2013).

[92] A. M. Carrascosa, M. Yang, H. Yong, L. Ma, A. Kirrander, P. M. Weber, and K. Lopata, Mapping static core-holes and ring-currents with X-ray scattering, Faraday Discuss. **228**, 60 (2021).

[93] S. Giri, G. Dixit, and J. C. Tremblay, Attosecond charge migration in heterocyclic five-membered rings, Eur. Phys. J.: Spec. Top. **232**, 1935 (2023).

[94] M. Vacher, L. Steinberg, A. J. Jenkins, M. J. Bearpark, and M. A. Robb, Electron dynamics following photoionization: Decoherence due to the nuclear-wave-packet width, Phys. Rev. A **92**, 040502(R) (2015).

[95] M. Vacher, M. J. Bearpark, M. A. Robb, and J. P. Malhado, Electron dynamics upon ionization of polyatomic molecules: Coupling to quantum nuclear motion and decoherence, Phys. Rev. Lett. **118**, 083001 (2017).

[96] C. Arnold, O. Vendrell, and R. Santra, Electronic decoherence following photoionization: Full quantum-dynamical treatment of the influence of nuclear motion, Phys. Rev. A **95**, 033425 (2017).